Liu *et al. Green Manuf Open* 2023;1:12
DOI: 10.20517/gmo.2023.03

Green Manufacturing Open

Research Article

Open Access

Numerical analysis on flow and surface topography of the molten pool in laser additive remanufacturing

Weiwei Liu[1,2], Yongxin Zhao[1], Huanqiang Liu[1], Bingjun Liu[1], Tao Li[1], Shujie Liu[1]

[1]School of Mechanical Engineering, Dalian University of Technology, Dalian 116024, Liaoning, China.
[2]State Key Laboratory of High-performance Precision Manufacturing, Dalian University of Technology, Dalian 116024, Liaoning, China.

Correspondence to: Prof. Weiwei Liu, School of Mechanical Engineering, Dalian University of Technology, No.2 Linggong Road, Ganjingzi District, Dalian 116024, Liaoning, China. E-mail: liuww@dlut.edu.cn

How to cite this article: Liu W, Zhao Y, Liu H, Liu B, Li T, Liu S. Numerical analysis on flow and surface topography of the molten pool in laser additive remanufacturing. *Green Manuf Open* 2023;1:12. https://dx.doi.org/10.20517/gmo.2023.03

Received: 4 Apr 2023 **First Decision:** 8 May 2023 **Revised:** 30 May 2023 **Accepted:** 21 Jun 2023 **Published:** 30 Jun 2023

Academic Editor: Haihong Huang **Copy Editor:** Dong-Li Li **Production Editor:** Dong-Li Li

Abstract

Laser additive remanufacturing technology is an important technology in the field of manufacturing technology innovation and development, which has largely revolutionized the design and manufacturing mode of high-end devices to a large extent, and is a key component of green remanufacturing that can effectively promote the sustainable and sound development of the manufacturing industry. A multiphase model of laser additive remanufacturing with pulsed lasers is developed to analyze the evolution of the molten pool, the trend of the surface tension for different process parameters, and their relation to the molten pool morphology. The results demonstrate that the maximum flow velocity at the surface of the molten pool is inversely proportional to the pulsed laser frequency and to the duty ratio. While the trend of the height of the cladding layer corresponds to the trend of the heat accumulation in the molten pool, the width and penetration depth of the cladding layer are governed by the size of the heat-affected zone. The cladding layer and substrate will have poor metallurgical bonding if the pulsed laser frequency is too high. When the duty ratio is too large, the likelihood of over-melting increases, affecting the substrate properties and increasing the surface roughness, which is detrimental to the surface finish of the cladding layer.

Keywords: Laser additive remanufacturing, pulsed laser, numerical simulation, molten pool flow

INTRODUCTION

Laser cladding (LC) is one of the main technologies for laser additive remanufacturing, which uses a high-power laser beam as a heat source[1]. It radiates the substrate and powder, causing them to melt and solidify simultaneously, creating a cladding layer on the substrate surface. This is an essential aspect of laser additive remanufacturing technological breakthroughs[2,3]. Currently, it has a wide range of applications in high-tech fields, such as aviation, aerospace, and automobiles.

The rapid and continuous phase shift of the metal from solid to liquid to solid is caused by a pool of molten metal generated by the local heat input during laser additive remanufacturing. There are phenomena such as heat transmission and convection, such as powder melting, melt flow[4], and solidification[5], that occur from the start of the deposition until the completion of the workpieces[6]. The homogeneity and compactness of the material structure are directly affected by the hydrodynamic behavior of the molten pool[7], and the generation and control of the molten pool are one of the main parts of the laser additive remanufacturing process. Most scholars establish the connection between them through analysis[8], mathematical models[9], monitoring[10], or numerical simulation[11].

At the same time, the laser processing parameters differ, as do the end part characteristics produced[12,13]. Pinkerton and Li found a link between the width and frequency of the laser and the surface roughness of the sample. Pulse beams can minimize porosity. However, lower pulsed frequencies result in rougher surfaces. As the pulsed frequency rises, so does the final hardness of the 316L stainless steel. Shi *et al.* used regression algorithms to create a mathematical model, investigated the relationship between laser power, scanning speed, additional parameters, and the geometry of the cladding layer, and then used the mathematical model to predict the geometric characteristics of the cladding layer[9]. Xing *et al.* obtained the temperature distribution and molten pool size by varying several laser process parameters while also considering the effect of material state transitions and the heat source model[14]. It was found that an increase in laser power and a decrease in scanning speed both lead to an increase in the maximum powder layer temperature and an increase in molten pool size, and it was also revealed that the heat source model must be determined according to the size of the element. Yazar *et al.* investigated the effects of laser power and scanning speed on the roughness, cladding layer morphology, microstructure, texture, and hardness of single-layer deposited 316L surfaces[15]. It was observed that the surface roughness is inversely proportional to the laser power and that the hardness is almost insensitive to the treatment parameters. Wu *et al.* established an ensemble of metamodels (EM), studied the relationship between laser process parameters (laser power, scan speed, and defocusing amount) and three outputs (total energy consumption, surface roughness, and depth-width ratio of LST track), and predicted the optimal combination of process parameters, which provided a reliable basis for energy sensing applications in laser processing[16].

The flow dynamics[17] and geometric evolution[18] of the liquid molten pool are firmly correlated with the deposition size, molten pool shape[18], mechanical quality[19,20], and surface quality[21,22] of the additive remanufactured material[23,24]. Song *et al.* proposed a phase-consistent molten pool edge extraction method to obtain more accurate molten pool geometry and developed a real-time molten pool monitoring system to monitor geometric changes and time-varying molten pool evolution[25]. Gharbi *et al.* found that using a strong average power can increase surface finish but that using a quasi-continuous pulse mode rather than full continuous laser heating is also an effective technique to improve surface finish[26]. Gharbi *et al.* established a simple mathematical model that connected the geometry of the molten pool with the surface polish and demonstrated that the remelting process improved the roughness characteristics[27]. Tang *et al.* proposed a real-time prediction approach based on coaxial visual features and the convection state of the molten pool, which predicted the penetration depth via the convection zone of the molten pool monitored

by coaxial vision[28]. Using finite element analysis, Ding *et al.* were able to simulate the time evolution of temperature distribution in a single run[29]. They studied the geometry of the simulated molten pool and found that the width and depth of the pool increased as the laser energy grew. Bhatnagar *et al.* proposed a lumped parametric model that predicts the molten pool temperature, the cladding geometry, and the dilution of the substrate, taking into account the energy transfer and loss mechanisms and the surface tension phenomena of the molten material[30].

To sum up, it can be seen that the methods used by most scholars to solve free surfaces in recent years are almost the same, and no matter which method is used, the finite element model can be better established, and the expected effect can be achieved. The very well-established Volume of Fluid (VOF) method in Fluent will be chosen to solve the free surface. In addition, it can be found that relatively perfect numerical simulation models of laser additive remanufacturing molten pool mainly focus on the study of molten pool flow behavior and mechanism of continuous laser, while there are few studies on the specific evolution process of molten pool in LC and the law of surface fluctuation, especially the law of molten pool flow under the pulsed laser is still unclear. The dynamic properties of the heat flow in the molten pool during the cladding process are directly related to the shape properties and internal microstructure properties of the formed layer. In addition, during the laser additive remanufacturing process, the surface of the molten pool changes, resulting in defects and spots around the molten pool. Moreover, the molten pool is very small, and the formation time is very short[31]. After monitoring, the extraction of the pool boundaries by various image processing algorithms, such as the fixed grayscale threshold method and the fuzzy entropy threshold method, is limited to a certain extent, and the entire formation and evolution of the pool cannot be detected. Thus, the transient molten pool can be analyzed by means of numerical simulations.

The Fluent software was used to convert laser energy into a Gaussian heat source, and the Volume fraction of phase[32] was introduced through the VOF model to solve the continuity equation. A multiphase finite element model of the pulsed laser additive remanufacturing process was developed to model the transient motion, heat transfer, and fluid flow of the molten pool. The influence of the pulsed laser frequency and duty ratio on the evolution and flow velocity of the molten pool has been studied. In combination with related experimental methods, a two-color pyrometer was used to monitor the temperature of the molten pool and measure the size and surface roughness. The variations in the size and surface mass of the molten pool at different pulsed laser frequencies and duty ratios were analyzed, and the accuracy of the numerical model was also verified.

METHODS

Experimental setup

The substrate and powder used for laser additive remanufacturing are both 316L stainless steel. Table 1 lists the relevant physical performance parameters.

The schematic diagram of the experiment and simulation is shown in Figure 1, Figure 1A is the experimental platform built, and Figure 1B is the temperature field at a certain moment during laser additive remanufacturing. The experiment uses a pulsed laser mode. The duty ratio is the ratio of the laser on time to the total time in a pulse cycle. The specifically designed duty ratio, pulsed laser frequency, and other laser processing parameters are listed in Table 2. The computational domain size of the 3D symmetric numerical model for laser additive remanufacturing is 10 mm × 3 mm × 3 mm, including the substrate and air domains [Figure 1B]. The laser is scanned in the positive x-direction.

Table 1. Parameters of 316L stainless steel[33]

Parameters	316L
Density/(kg·m^{-3})	7,200
Latent heat of fusion/(J·kg^{-1})	2.67 × 10^{5}
Temperature coefficient of surface tension/(N·m^{-1}·K^{-1})	-4 × 10^{-4}
Dynamic viscosity/(kg·m^{-1}·s^{-1})	6.76 × 10^{-3}
Thermal expansion coefficient/ K^{-1}	1.9 × 10^{-5}
Solidus temperature/K	1,693
Liquidus temperature/K	1,733
Initial temperature/K	300 K
Gravitational acceleration/(m/s^{2})	9.81

Table 2. Variation of process parameters

	Laser power	Scan speed/ mm·s^{-1}	Powder feeding rate /g·min^{-1}	Shielding gas flow / L·min^{-1}	Duty ratio	Pulsed laser frequency /Hz
Pulsed laser frequency variation	1,400	6	9.15	15	1:1	13.33
						20
						25
						50
Duty ratio variation	1,400	6	9.15	15	1:1	13.33
					2:1	
					3:1	
					4:1	

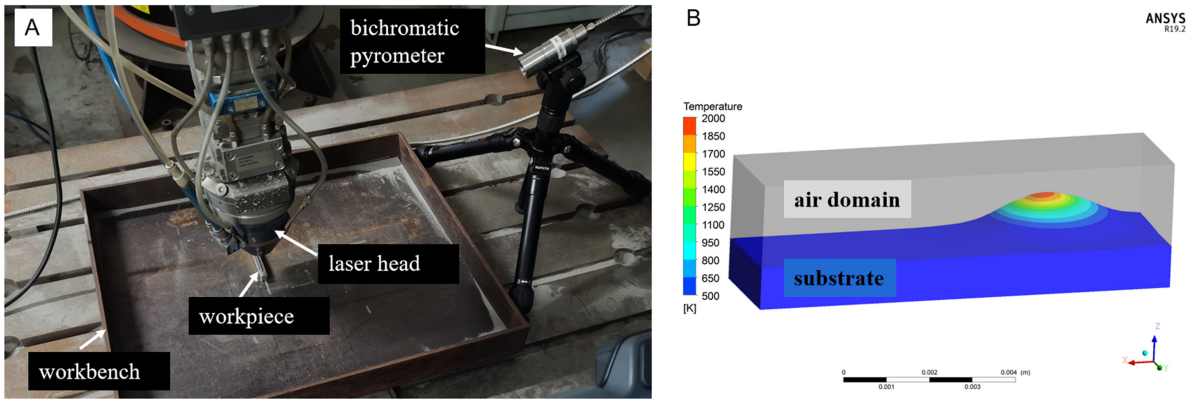

Figure 1. Experiment and simulation schematics. (A) Experimental schematic diagram; (B) simulation schematic diagram.

Figure 2 depicts the specific equipment used for the laser additive remanufacturing experiment. The laser beam is generated by a semiconductor laser. At the same time, argon gas is used to transport the metal powder to the substrate through a feeding tube. The laser melts the powder, creating a molten pool that gradually solidifies into a cladding layer. A six-axis robot performs a moving scan of the laser head until the full laser additive remanufacturing process is completed. The following is a list of equipment and parameters:

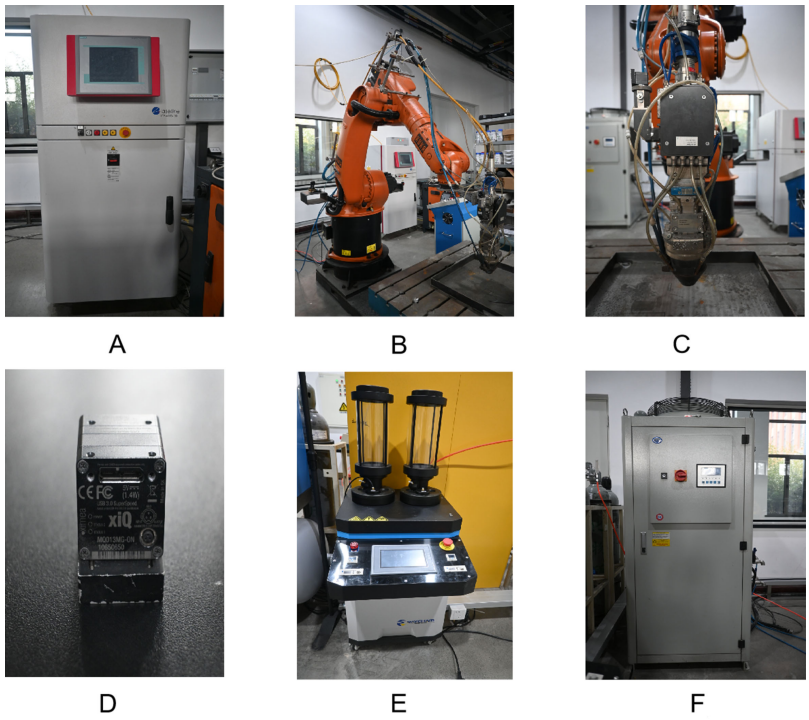

Figure 2. Diagram of experimental laser additive remanufacturing equipment. (A) Semiconductor laser; (B) six-axis robot; (C) coaxial laser head; (D) CMOS camera; (E) carrier gas powder feeder; (F) laser water cooler.

Semiconductor laser: LDF 4000-100 produced by German Laserline company, mainly including laser head, energy supply, cooling module, control system, and touch control panel, as shown in Figure 2A, the minimum fiber diameter can reach 1,000 μm and generate up to 4,400 W of laser power.

Six-axis robot: the model is KUKA KR30HA, and the equipment has 6 CNC axes, as shown in Figure 2B; the distance can reach 2,233 mm, the total load is 65 kg, the payload is 30 kg, the finite element method is used to achieve high precision operation, and the position repeatability is ±0.06 mm.

Coaxial laser head: precitec YC52, ideal for fiber-guided lasers in the medium to high power range, as shown in Figure 2C, with four beam nozzles, a powder focus diameter of 2 mm, and a working distance of 15 mm. As illustrated in Figure 2D, a coaxial CMOS camera is mounted on the axis of the laser head to monitor the dynamic properties of the molten pool in real time.

Carrier gas powder feeder: the double-barrel carrier gas powder feeder with model RC-PGF-D2, as shown in Figure 2E, can realize long-distance synchronous powder transportation and carry nitrogen and argon gas.

Laser water cooler: this is an MCWL device made by Tongfei. It is entirely controlled by the CPU, as shown in Figure 2F, with a water temperature control accuracy of ±1 °C and the ability to diagnose, and the temperature was fixed at 15 to 50 °C.

Temperature monitoring of the molten pool

A two-color pyrometer was used to monitor the experimental temperature. It adopts Sensortherm Metis M322, as shown in Figure 3, which is placed next to the workbench [Figure 1A], and its measurement range varies with the distance from the workpiece, and the correlation is illustrated in Table 3. The minimum monitoring distance is employed for temperature recording for the desirability of the experimentally recorded temperature, the measurement temperature range is 1,000-3,300 °C, and the temperature below 1,000 °C is presented as 1,000 °C.

Size extraction of the molten pool

The molten pool created by laser additive remanufacturing is typically 0.5-3 mm in diameter[30], and the molten pool is fairly tiny. The molten pool size cannot be accurately measured using a regular vernier caliper or other measuring devices. It is necessary to mount and polish the laser additive remanufacturing processing sample and observe and photograph its cross-sectional morphology with a super-depth-of-field microscope (VHX-600E03041132). Samples before and after polishing are shown in Figure 4.

The instrument used for surface roughness measurements is the OLS4000 laser confocal microscope. The measurement process and the apparatus are shown in Figure 5. The total length of the cladding layer of the sample piece is 40 mm, except for the head and tail parts, where 20 mm in the middle deposition process is selected to measure the surface line roughness, as shown in Figure 5B. Laser confocal microscopy divides this line into different blocks, each of which performs a roughness calculation and recording and finally calculates the mean value of the roughness Ra of the line.

Simulation model

Geometric model

To better study the virial morphology of the molten pool and the fluid flow inside the molten pool, a 3D numerical model was developed. Considering a large number of 3D calculations, a half-computational domain in the Y-direction is used to save computation time, as shown in Figure 6. The total calculation domain size is 10 mm × 3 mm × 6 mm, containing the substrate and air domain; the size of the substrate is 10 mm × 3 mm × 2 mm, and the size of the air domain part is 10 mm × 3 mm × 4 mm.

A mesh is a non-uniform, fixed, and unstructured mesh. In this paper, the meshing is performed using ICEM, where the unstructured mesh is partitioned by setting the number of nodes at the boundary and subsequently mapped to the entire computational domain. The hexahedral mesh chosen allows for a better calculation of the surface tension effect. To meet the requirements of the numerical simulations, the minimum mesh size in the intermediate region, where melting and solidification occur, is 0.05 mm. This mesh size ensures the accuracy and stability of the solution of the continuity and transport equations. Smaller grids do not change the results much but increase the computation time. The mesh is relaxed elsewhere to save computational time. The total number of meshes for the entire computational domain is 114,900.

VOF model

Laser additive remanufacturing is a complex transient process. Under the assumption that the accuracy of the numerical simulation results is satisfied, the mathematical model of this study makes the following assumptions:

1. The laser beam is assumed to follow a Gaussian distribution;

Table 3. Measurement distance and temperature range

Measurement distance/mm	Measurement range diameter/mm	
	Temperature/300-1,000 °C	Temperature > 1,000 °C
240	2	1
300	2.5	1.5
400	3	2
500	3.7	2.5
600	4.5	3
800	6	4
1,000	7.7	5
1,500	11.5	7.5
2,000	15.4	10
2,500	19.2	12.5
3,000	23	15

Figure 3. Two-color pyrometer.

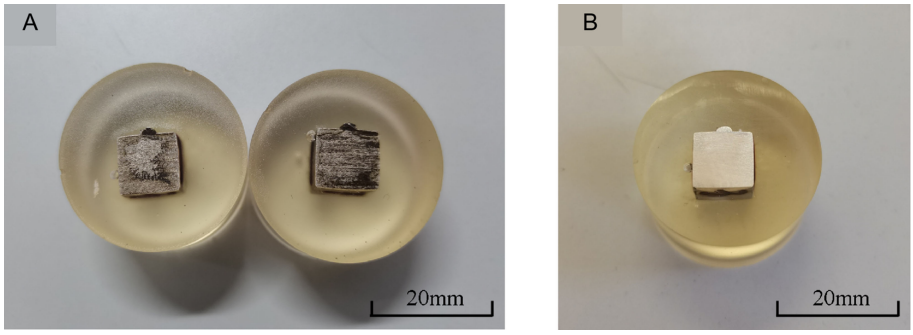

Figure 4. Processing sample. (A) Unpolished; (B) polished.

2. Liquid metal is considered to be an incompressible Newtonian fluid, and the flow in a pool of molten metal is laminar;

3. The fluid flow is driven by the buoyancy in the molten pool and the surface tension of the molten pool;

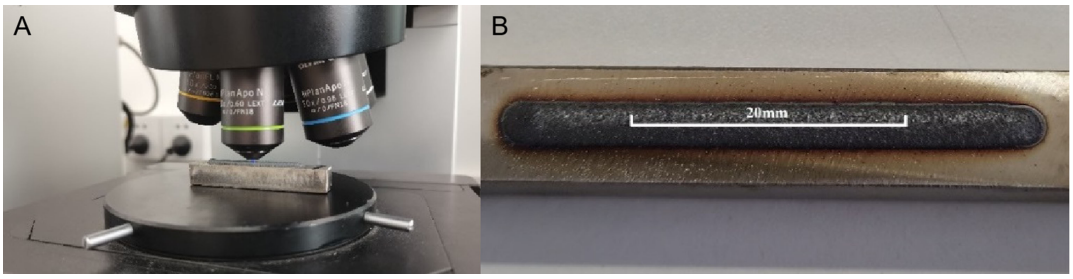

Figure 5. Roughness measurement. (A) OLS4000 confocal laser microscope; (B) measuring length.

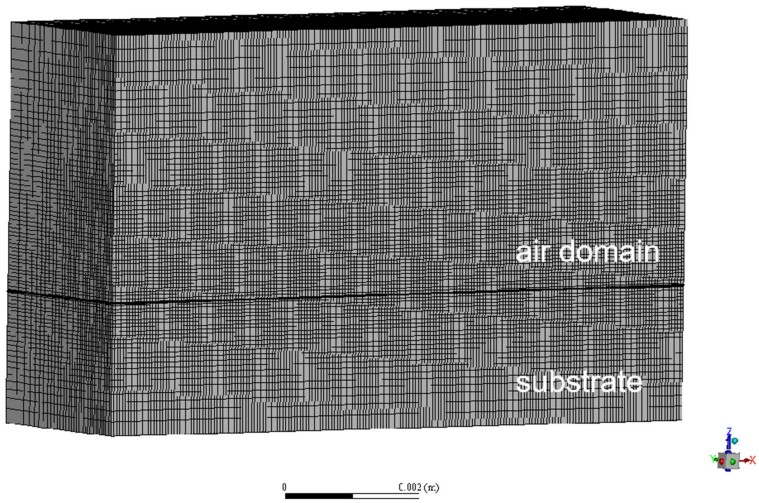

Figure 6. Three-dimensional mesh model.

4. With the exception of the thermal conductivity and specific heat capacity, the other thermal physical parameters are constant and independent of temperature;

5. The substrate and the powder material are continuous and homogeneous.

In the VOF model, the tracing of the phase interface is achieved by introducing a variable for the volume fraction of the phase. Within each control volume, the volume fractions of all phases sum to one. In the unit, the fluid volume fraction of the "q" phase may appear in the following three situations:

1. $\alpha_q = 0$, the unit does not have the "q" phase liquid;

2. $\alpha_q = 1$, the unit is filled with the "q" liquid;

3. $0 < \alpha_q < 1$, the unit contains the interface between the fluid and one or more other fluids.

Based on the value of α_q, appropriate attributes and variables will be assigned to each control volume in the domain.

The tracking of the interface between the phases is achieved by solving the continuity equation of one (or more) phase volume fractions. For the "q" phase, the form of the equation is Equation (1)[34].

$$\frac{\partial \alpha_q}{\partial t} + v \cdot \nabla \alpha_q = 0 \tag{1}$$

In the formula, α_q is the fluid volume fraction of the "q" phase, and v is the fluid velocity. The calculation of the volume fraction of the main phase is based on the following constraints in Equation (2)[34]:

$$\sum_{q=1}^{n} \alpha_q = 1 \tag{2}$$

Governing equations

At the core of numerical simulations of laser additive remanufacturing is the transport of energy and heat in a molten bath. The mass transfer, heat transfer, and fluid flow of the molten pool are respectively controlled by the conservation of mass, conservation of energy, and momentum equations, and the expressions are Equation (3), Equation (4), and Equation (5)[34]:

$$\frac{\partial \rho}{\partial t} + \nabla(\rho v) = S_{mass} \tag{3}$$

$$\frac{\partial H}{\partial t} + H\nabla v = \frac{1}{\rho}(\nabla \cdot k\nabla T) + \frac{h_s}{\rho} + S_{energy} \tag{4}$$

$$\frac{\partial v}{\partial t} + v\nabla v = \mu\nabla v - \frac{1}{\rho}\nabla p + g + S_{mom} \tag{5}$$

Where ρ is the metal density, t is the time, and v is the fluid velocity; H is the enthalpy, k is the thermal conductivity, and h_s is the enthalpy increment of the external filling material; P is the pressure, g is the acceleration due to gravity, and μ is the viscosity; S_{mass} is the mass source term, S_{energy} is the energy source term, and S_{mom} is the momentum source term.

Initial boundary conditions

Initial conditions:

To solve the control equation of the temperature field, the initial temperature conditions can be considered as follows[35]:

$$T(x, y, z, t = 0) = T_0 \tag{6}$$

T_0 is the initial temperature of the metal powder and the substrate, and T_0 = 300 K.

Boundary conditions:

There are five boundary conditions contained in the entire computational domain: the symmetrical boundary surface of the symmetric model; the remaining three sides of the substrate; the underside of the substrate; the interface between the substrate and the air domain; the remaining four air domain interfaces.

Symmetric boundary conditions are used first when the physical geometry and the expected flow/thermal solution pattern are mirror symmetric. The flow in the laser additive remanufacturing molten pool is symmetric around the z-axis in a plane perpendicular to the laser scan direction, which is suitable for symmetric boundary conditions. As shown in Figure 7, the gold surface is an antisymmetric boundary surface. The normal gradient of all flow variables is 0 in the plane of symmetry. That is[36]:

$$\vec{v}_{sn} = 0 \tag{7}$$

$$\vec{G}_{sn} = 0 \tag{8}$$

On three sides of the substrate, there is no thermal radiation, but there is convective heat transfer with air. In this study, the convective heat transfer in the solid wall boundary condition is set to three edges. Fluent uses the external heat transfer coefficient and the temperature of the external radiator to compute the heat flux at the wall when specifying boundary conditions for the convective heat transfer coefficient at the wall. The formula is as follows[36]:

$$q_1 = h\left(T - T_0\right) \tag{9}$$

Where q_1 is the wall heat flux, h is the convective heat transfer coefficient, and T is the real-time wall temperature.

The bottom surface of the substrate was placed on a workbench, and the thickness of the substrate and the thickness of the cladding were experimentally separated by order of magnitude. It is assumed that there is no heat exchange at the bottom surface of the substrate; that is, the heat flux is zero. The heat current is set to 0, and the solid wall boundary conditions are still specified.

The laser immediately affects the interface between the substrate and the air domain, leading to both convective and radiative heat transfer. Here is the heat transfer formula[36]:

$$q_2 = h\left(T - T_0\right) + \varepsilon\sigma\left(T^4 - T_0^4\right) \tag{10}$$

Where q_2 is the wall heat flux, ε is the surface emissivity, and σ is the Stefan Boltzmann constant.

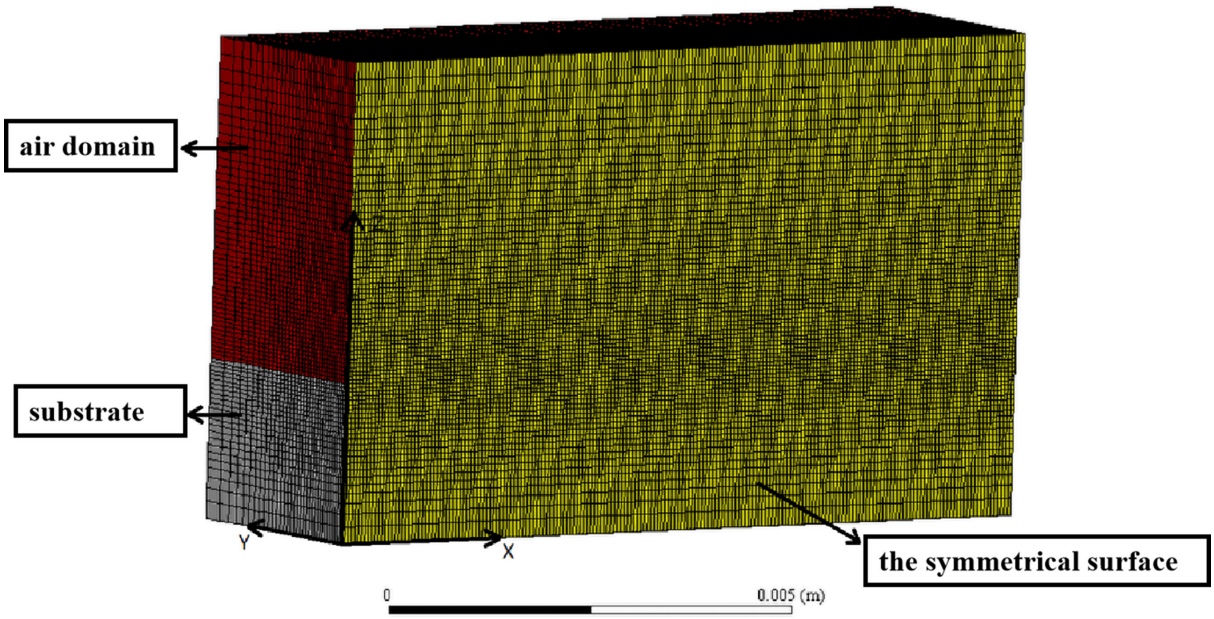

Figure 7. Initialized model.

The remaining four interfaces of the air domain are the interfaces between the external environment of the air domain. The pressure outlet boundary condition is set because the injection of shielding gas causes air to flow inside the air domain and exchange air with the outside world. Figure 7 depicts the finished initialized model.

Model validation

A comparison of the cross sections for the pulsed LC experiment and the simulation is shown in Figure 8. In numerical simulations, the cladding layer has a height of 0.651 mm, a width of 3.312 mm, and a penetration depth of 0.147 mm. The relative errors are 7.07%, 14.36%, and 6.52% for the measured deposition height of 0.608 mm, width of 2.896 mm, and penetration depth of 0.138 mm, respectively. Since the numerical model data is accurate within tolerable limits, the initial model is a better alternative to the experimental results.

Figure 9 shows a comparison between the simulated and actual pyrometer-measured temperatures at a fixed location on the sediment layer surface. The yellow curve in Figure 9 shows the results of the numerical simulations, and the blue curve shows the experimental measurements, indicating a strong agreement between the experimental and simulated results. The relative errors between the actual measured and simulated temperatures range from 0.82% to 28.50%, respectively. Once again, the bias is caused by the inaccurate numerical simulation of the utilization of the laser heat source.

RESULTS AND DISCUSSION

Analysis of the molten pool flow

Evolution of the molten pool at different pulsed laser frequencies

Figures 10-12 show the evolution of the melting pool over time at various pulsed laser frequencies, with black arrows indicating the direction and magnitude of the liquid metal flow. The chosen time duration for the various frequencies is around 0.3 s. The temperature cloud map of surface y = 0 (mm) shows that as the

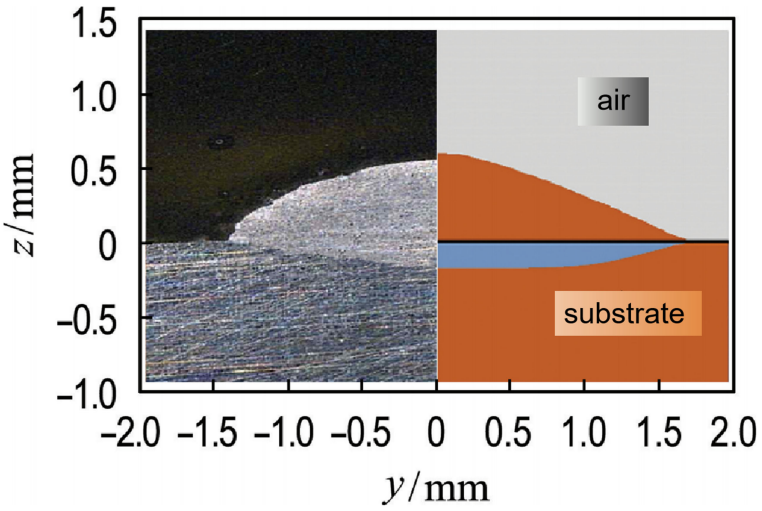

Figure 8. Cross-section contrast.

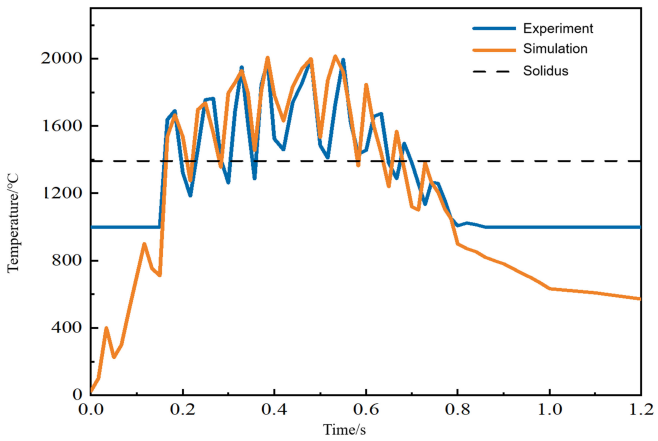

Figure 9. Temperature change at a fixed location.

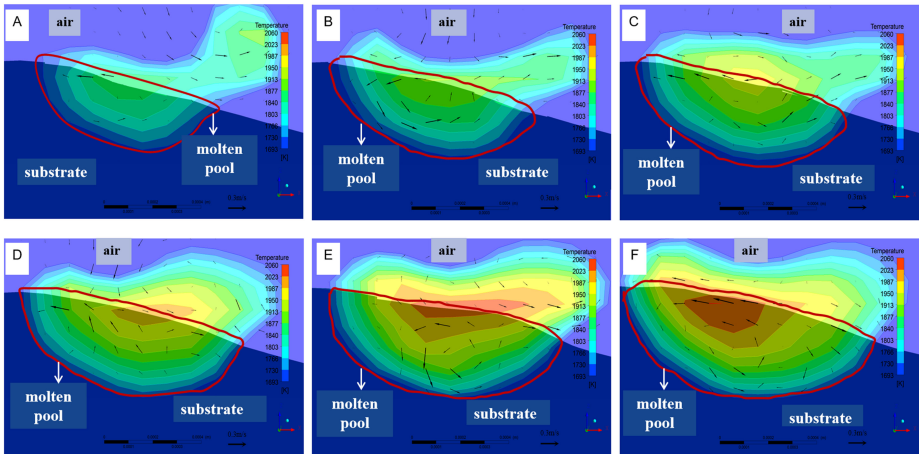

Figure 10. Flow of molten pool at 20 Hz frequency. (A) 0.306 s; (B) 0.308 s; (C) 0.310 s; (D) 0.312 s; (E) 0.316 s ; (F) 0.318 s.

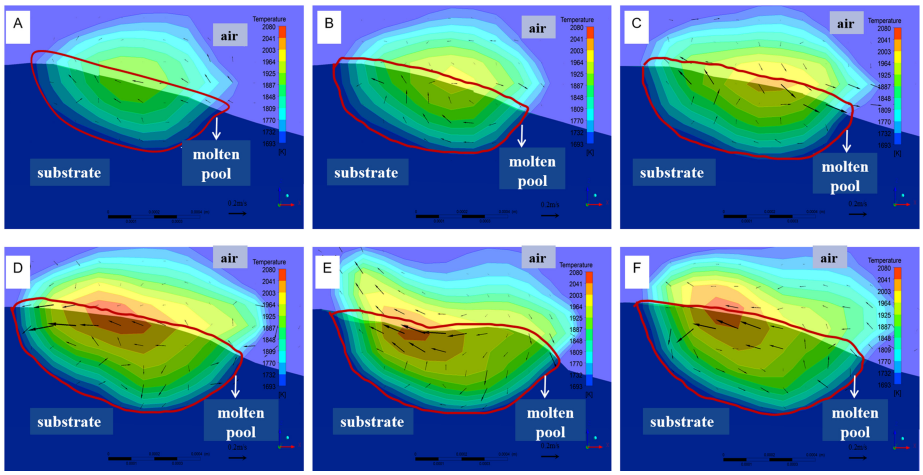

Figure 11. Flow of molten pool at 25 Hz frequency. (A) 0.290 s; (B) 0.293 s; (C) 0.296 s; (D) 0.299 s; (E) 0.302 s; (F) 0.305 s.

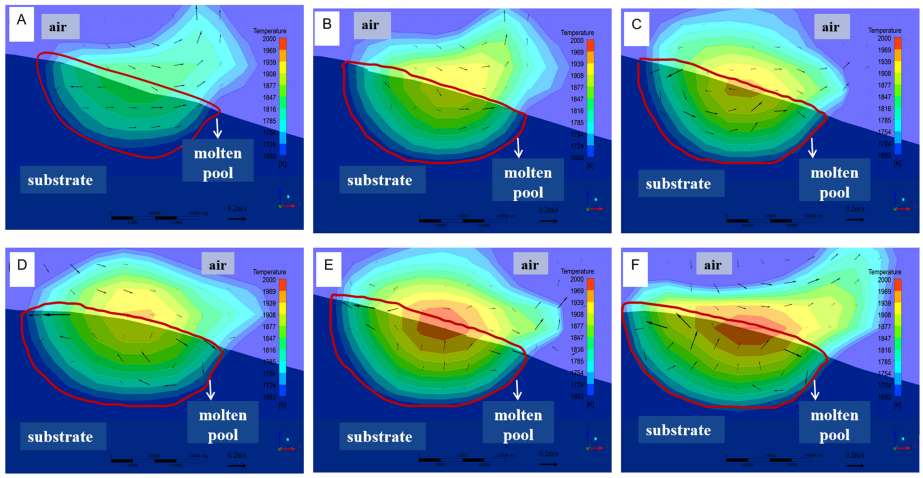

Figure 12. Flow of molten pool at 50 Hz frequency. (A) 0.302 s; (B) 0.303 s; (C) 0.305 s; (D) 0.306 s; (E) 0.308 s; (F) 0.309 s.

frequency rises, the final heat-affected zone shrinks, and the size of the molten pool shrinks. The shape evolves from a flat ellipse to a semicircle over time. The zone of thermal influence gradually expands as time passes and the laser propagates; however, as the pulsed laser frequency increases, the size of the heat-affected region, that is, the size of the molten pool, gradually decreases within the same time node. When the laser at each frequency is turned on, the flow velocity inside the molten pool increases progressively. The maximum flow velocity is found at the intersection of the liquid/gas interface and the edge of the molten pool when an annular flow circle is finally established.

Figure 13 depicts the dynamic change curves of the maximum flow velocity on the surface of the molten pool at various pulsed laser frequencies, demonstrating periodic variations, with denser variations at higher frequencies. The growth in Figures 13B and C is obvious, and it reaches the highest level of stability. The maximum flow velocity is 0.620 $m \cdot s^{-1}$ at 13.33 Hz, 0.608 $m \cdot s^{-1}$ at 20 Hz, 0.586 $m \cdot s^{-1}$ at 25 Hz, and 0.545 $m \cdot s^{-1}$ at 50 Hz. The maximum flow velocity at the surface of the molten pool steadily decreases as the frequency increases. This result is because the temperature differential is related to the driving force of the fluid flow in the molten pool, and the maximum temperature that the molten pool may achieve varies with frequency.

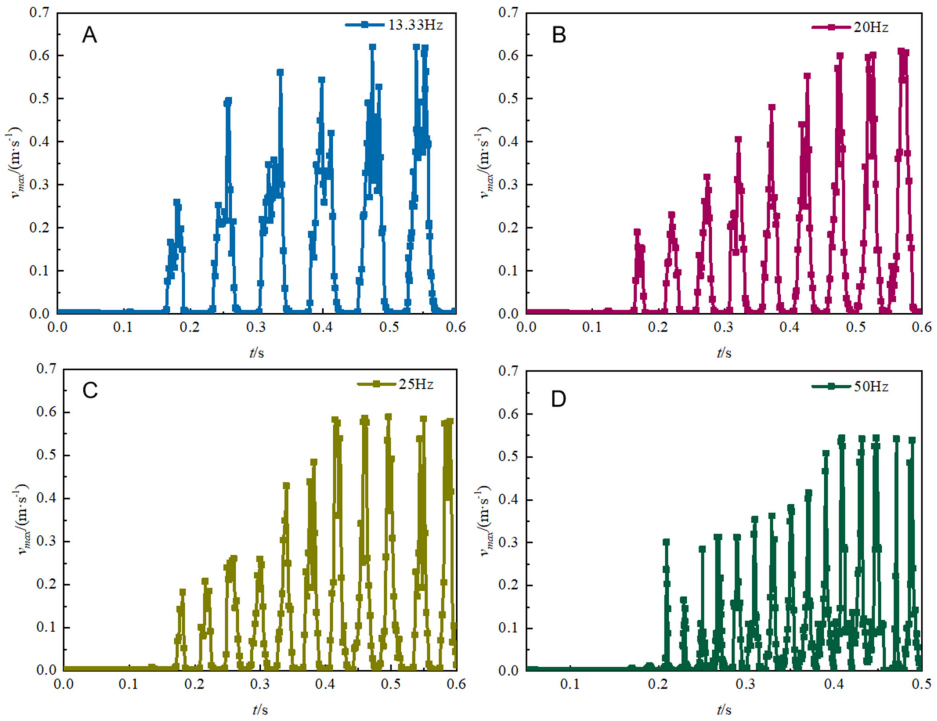

Figure 13. The maximum velocity variation of molten pool surface at different pulsed laser frequencies. (A) 13.33 Hz; (B) 20 Hz; (C) 25 Hz; (D) 50 Hz.

The maximum temperature of the molten pool is inversely proportional to the pulsed laser frequency. As the pulsed laser frequency increases, the temperature of the molten pool decreases so that its surface tension becomes larger, and its buoyancy and flow velocity become smaller. Simultaneously, when the pulsed laser frequency is 50 Hz, the surface flow velocity of the molten pool is extremely low before 0.2 s, and there is essentially no flow. This is due to the elevated pulsed laser frequency, the low heat input from the external laser heat source into the molten pool, the large surface tension, and the difficulty of liquid metal flow.

The main driving force for fluid flow in a molten pool is surface tension. This has an impact not only on the flow of molten slag at the surface but also on the size of the zone of thermal influence. The minimum surface tension of the molten pool for each cycle under various process parameters is computed, as illustrated in Figure 14, for subsequent analysis to summarize the size and flow of the heat-affected zone under various frequencies. Since liquid metal has a lower surface tension, it flows more easily. The surface tension is inversely proportional to the temperature, as seen in Figure 14, so the lowest surface tension is found in the middle of the molten pool, where the temperature is highest. Combined with the flow direction of the Marangoni flow, the heat-affected zone is smaller when the surface tension in the middle of the molten pool is lower. The surface flow rate is lower, less heat is transmitted out, and the heat-affected zone is smaller, affecting the width of the cladding layer [Figure 15].

A super-depth microscope captured the morphology of the cladding layer at different frequencies in Figure 16. When combining Figure 16 and Table 4, it can be seen that as the pulsed laser frequency rises, the height of the cladding layer first rises and then falls while the width and penetration depth decrease. Meanwhile, the equivalent dilution rates for 13.33 Hz, 20 Hz, 25 Hz, and 50 Hz were 18.50%, 14.76%, 10.61%, and 3.04%, respectively. The dilution rate is calculated using the single-track cladding dilution rate formula:

$$\eta' = \frac{S_2}{S_1 + S_2} = \frac{\frac{2}{3}Wh}{\frac{2}{3}W(H + h)} = \frac{h}{H + h} \tag{11}$$

Where W is the width of the cladding layer, H and S_1 represent the height and area of the cladding layer, and h and S_2 represent the depth and area of the substrate after melting, respectively.

Since the powder has a Gaussian spatial distribution, the trend in the height of the cladding layer corresponds to the trend in the heat accumulation in the molten pool. The more heat that builds up in the molten pool, the more likely the powder will melt and the higher the cladding. The size of the zone of thermal influence determines the width and penetration depth of the cladding layer. The area of the thermal zone shrinks steadily as the pulsed laser frequency rises within the same time node; at the same time, the higher the pulsed laser frequency, the less likely it is that the heat will escape from the center of the molten pool, limiting its zone of thermal influence. The width and penetration depth of the cladding layer decrease with increasing frequency.

The height, width, and penetration of the cladding layer [Figure 15] decrease slightly with increasing pulsed laser frequencies, as shown in Table 4. The higher the pulsed laser frequency, the smaller the penetration depth and the worse the metallurgical bond between the cladding layer and the substrate. At a pulsed laser frequency of 50 Hz, the metallurgical bonding effect between the cladding layer and the substrate is low, corresponding to a dilution rate of only 3.04%. However, when the dilution rate is too low, the cladding layer and the substrate do not mix sufficiently, which affects the final mass of the part. Therefore, the pulsed laser frequency must not be higher than 50 Hz.

Evolution of the molten pool at different duty ratios

Figures 17-19 depict the evolution of the molten pool over time with a pulsed laser frequency of 13.33 Hz and varying duty ratios. Due to the constant input of laser heat into the molten pool, the heat-affected zone continues to grow as the deposition progresses. At the same time, the shape of the molten pool is more elongated than the shapes described earlier at different frequencies, and the shorter the laser turn-on time, the closer the molten pool approaches a semicircular shape; the longer the laser is turned on, the flatter the molten pool becomes. This result is because as the laser turn-on duration grows, the molten pool absorbs more heat, melting more liquid metal and broadening the range of effects. From this, it is inferred that the larger the duty ratio, the larger the zone of thermal influence.

At a pulsed laser frequency of 13.33 Hz and for various duty ratios, Figure 20 depicts the dynamic change curves of the maximum flow velocity on the surface of the molten pool. The interval of the change period gradually decreases as the duty ratio increases. Since the temperature rise is a process with a duty ratio of 3:1 or 4:1, the number of change cycles within 0-0.6 s is one more than in the case of a 1:1 or 2:1 duty ratio. As the duty ratio increases, the cooling time of the molten pool decreases, the base temperature of the molten pool increases before the start of the next cycle, and it becomes easier to reach the metallic liquid to form the molten pool first.

When the pulsed laser frequency remains constant at 13.33Hz, the maximum flow velocity on the molten pool surface is 0.620 $m \cdot s^{-1}$ when the duty ratio is 1:1, 0.628 $m \cdot s^{-1}$ when 2:1, 0.635 $m \cdot s^{-1}$ when 3:1, and 0.641 $m \cdot s^{-1}$ when 4:1. The maximum flow velocity at the surface of the molten pool depends on the duty ratio. As the heat input from the external laser heat source into the molten pool grows with the duty ratio,

Table 4. Sedimentary layer size values at different frequencies

Pulsed laser frequency /Hz	*H*/mm	*W*/mm	*h*/mm	Dilution rate
13.33	0.608	2.896	0.138	18.50%
20	0.612	2.835	0.106	14.76%
25	0.616	2.797	0.073	10.60%
50	0.604	2.654	0.019	3.05%

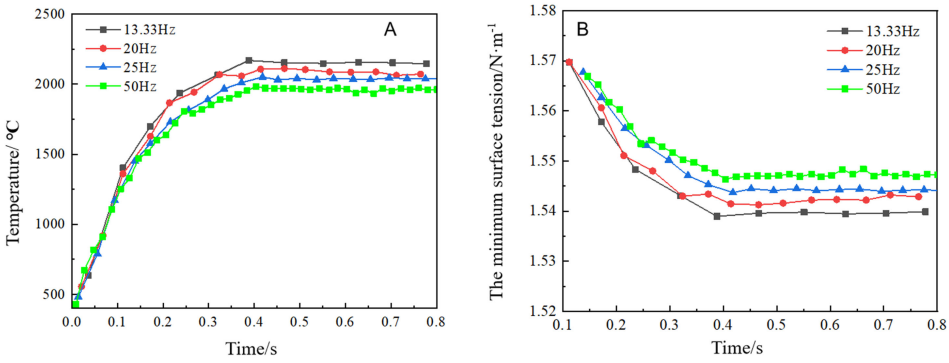

Figure 14. During each cycle at different frequencies. (A) The maximum temperature change of the molten pool; (B) the minimum surface tension of the molten pool.

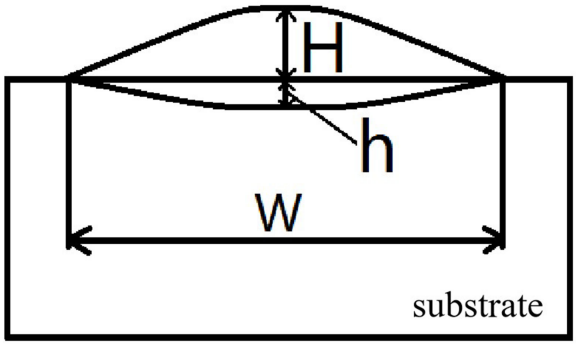

Figure 15. A diagram of the size of a molten pool.

the temperature increases, the surface tension holding the melt in place decreases, and the flow velocity increases.

Figure 21 shows that while the pulsed laser frequency is constant, the minimum surface tension in each cycle is inversely proportional to the duty ratio because the maximum temperature that a molten pool can achieve for a week rises with an increasing duty ratio. The higher the temperature, the greater the minimum surface tension. However, while there is a variation in the minimum surface tension, it is not significant. The Marangoni flow itself transports the heat out of the center. The higher the minimum surface tension, the less heat is transferred outwards, and the area affected by the heat becomes smaller, which is a relatively significant factor affecting the width of the cladding layers.

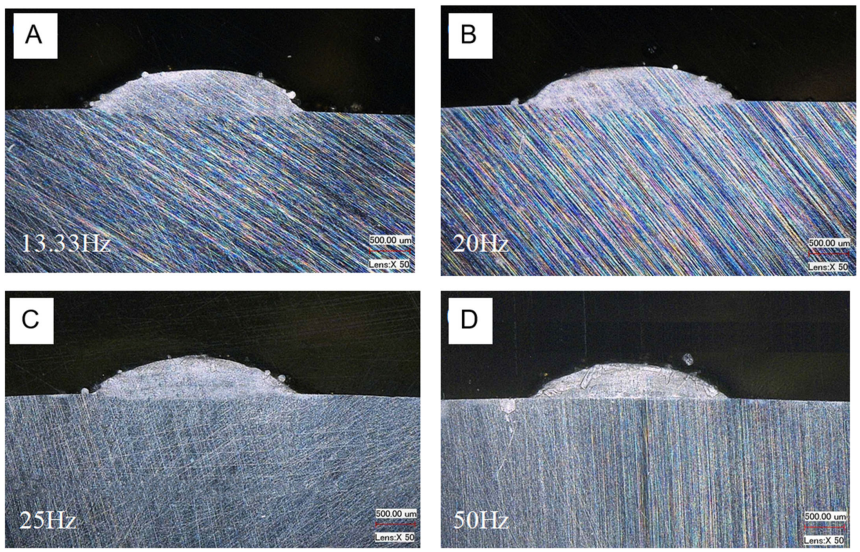

Figure 16. Morphology of the cladding layer at different frequencies.

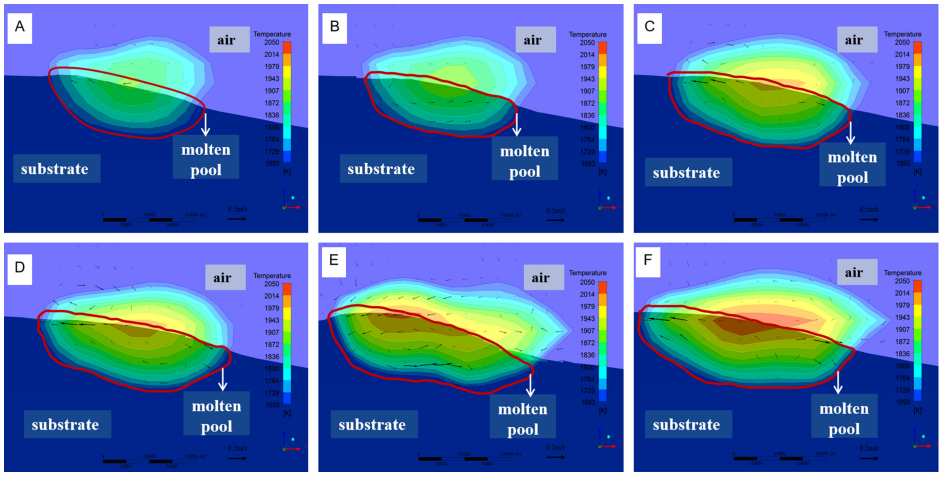

Figure 17. Flow of molten pool when duty ratio is of 2:1. (A) 0.306 s; (B) 0.310 s; (C) 0.316 s; (D) 0.320 s; (E) 0.328 s; (F) 0.332 s.

When the pulsed laser frequency remains constant, with the increase of the duty ratio, the laser on time increases, allowing more heat to be injected into the molten pool by the laser; thus, the heat accumulation of the molten pool increases proportionally to the duty ratio. The shape of the cladding layer during various duty ratios is shown in Figure 22. Table 5 presents the specific values. It can be seen that as the duty ratio increases, the height, width, and penetration of the cladding layer increase by a certain amount, as does the dilution rate. The higher the duty ratio, the more heat is accumulated, and the more heat accumulated, the more powder is melted, increasing the size of the cladding layer. The zone of thermal influence grows steadily as the duty ratio increases within the same time node; the larger the duty ratio, the more heat is transferred to the edges, which increases the thermal shock, and the penetration depth increases with the duty ratio.

Curve fitting was performed on the numerical relation between duty ratio and dilution rate, as shown in Figure 23. When the duty ratio is infinite, a continuous laser mode is used with a dilution rate of 28.2%.

Table 5. Sedimentary layer size values at different duty ratios

Duty ratio	*H*/mm	*W*/mm	*h*/mm	Dilution rate
1:1	0.608	2.896	0.138	18.5%
2:1	0.617	2.931	0.151	19.6%
3:1	0.648	2.95	0.163	20.1%
4:1	0.667	2.984	0.189	22.0%

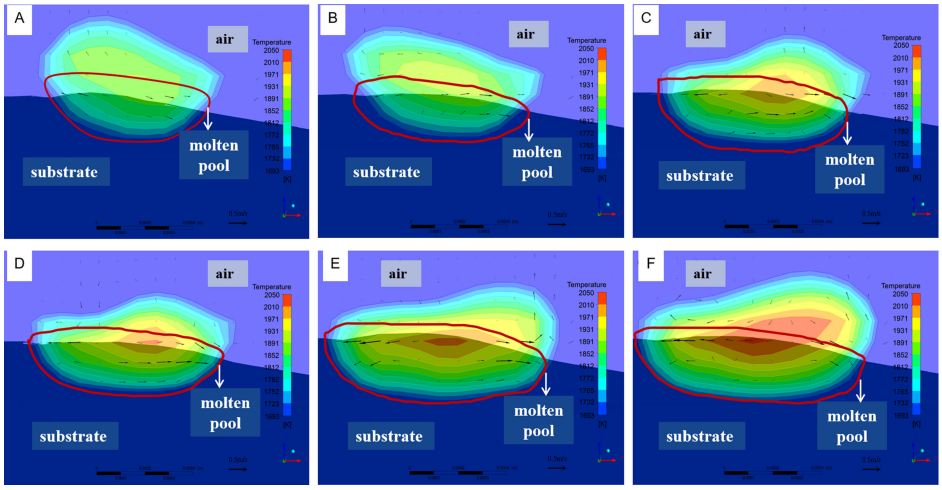

Figure 18. Flow of molten pool when duty ratio is 3:1. (A) 0.308 s; (B) 0.312 s; (C) 0.318 s; (D) 0.322 s; (E) 0.326 s; (F) 0.330 s.

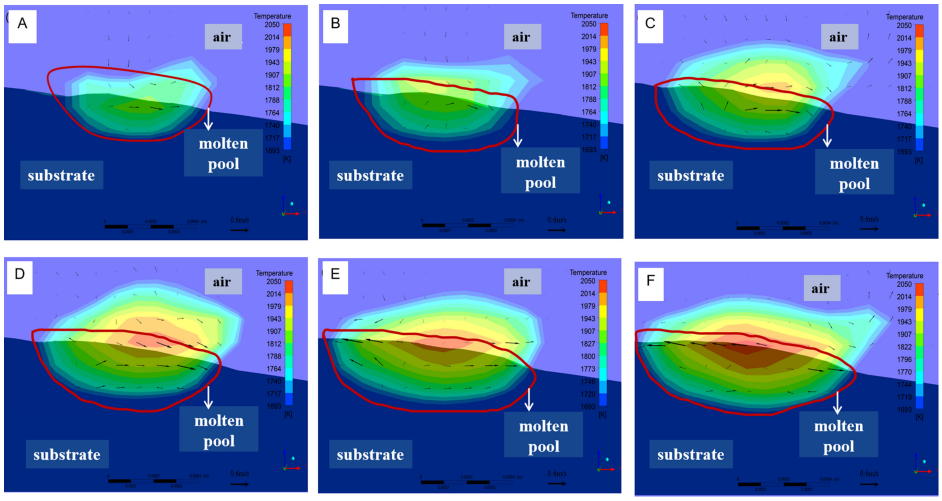

Figure 19. Flow of molten pool when duty ratio is 4:1. (A) 0.302 s; (B) 0.305 s; (C) 0.312 s; (D) 0.316 s; (E) 0.334 s; (F) 0.328 s.

When the dilution rate exceeds 30%, it has a significant impact on the metallic properties of the substrate, increasing the likelihood of fracture and deformation and reducing the performance of the cladding layer. The basic properties of the substrate can be maintained with a lower dilution rate. Based on the findings of the same group, the metallurgical bonding and processing performance of specimens with dilution rates in the range of 10%-20% was found to be excellent, with a duty ratio of less than 3:1 for pulsed LC at a laser power of 1,400 W.

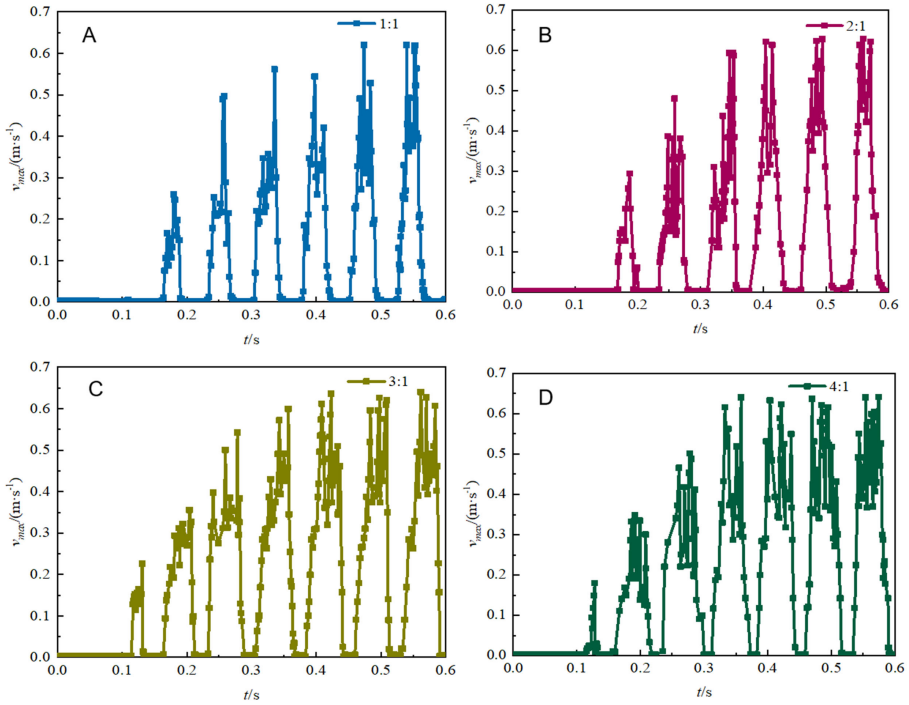

Figure 20. Variation of maximum flow velocity on molten pool surface at different duty ratios. (A) 1:1; (B) 2:1; (C) 3:1; (D) 4:1.

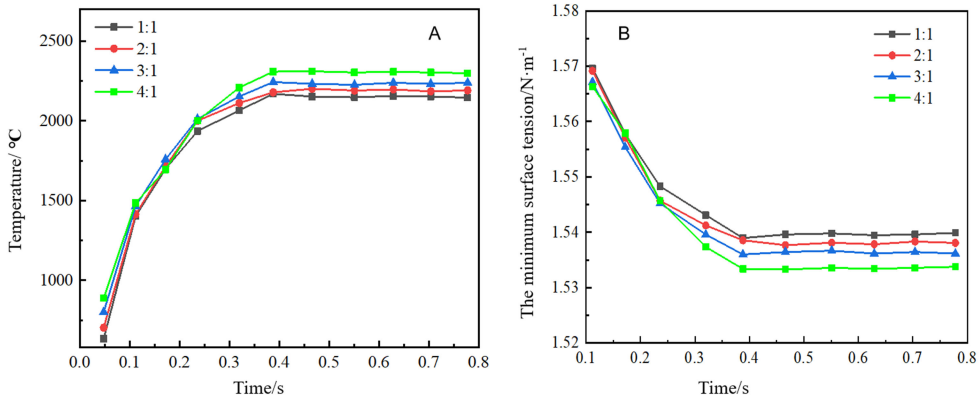

Figure 21. During each cycle at different duty ratios. (A) The maximum temperature change of the molten pool; (B) the minimum surface tension of the molten pool.

Analysis of surface topography and roughness

With a duty ratio of 1:1 and a pulsed laser frequency of 13.33 Hz, Figure 24 depicts the course of the slag trajectory in the 0.327-0.329 s range of the pulsed laser additive remanufacturing process. As the laser is switched on, the temperature rises to the greatest level, and some of the unmelted powder sticks to the surface of the cladding layer during the laser turn-off period, resulting in a larger amount of slag in the molten pool before the laser turn-on period, as illustrated in Figure 24A.

Figure 25 shows the evolution of the slag trajectory at the edge of the molten pool in the 0.540-0.542 s. After 0.002 s, the large molten slag on the bottom left side A and the upper right side B of the molten pool dispersed and contracted. As a result of the flow and surface fluctuations, some of the slag flows back into

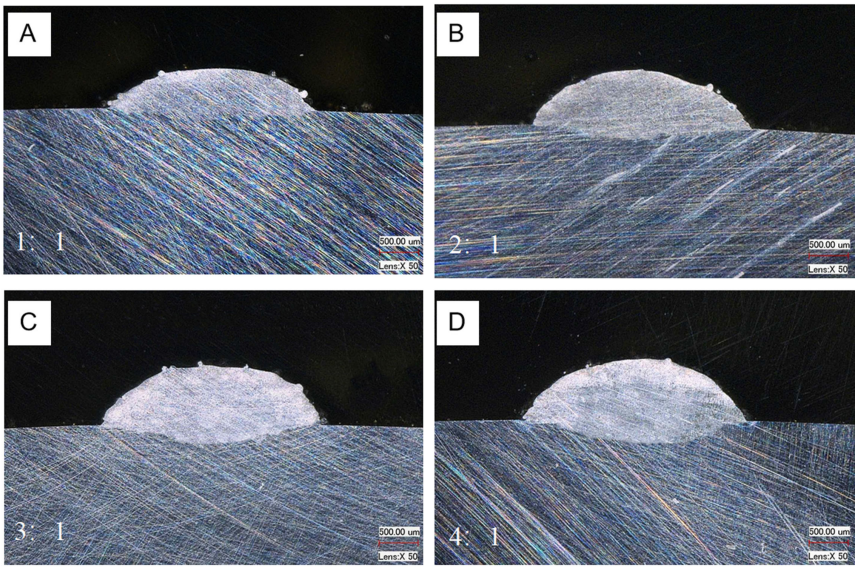

Figure 22. Morphology of the cladding layer at different duty ratios.

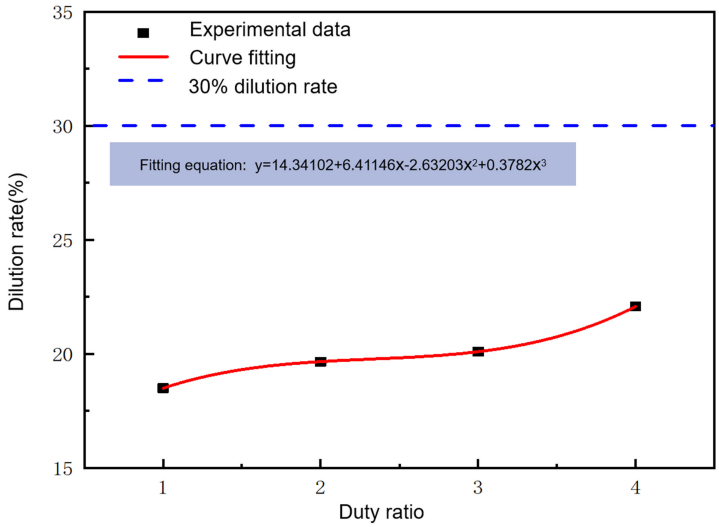

Figure 23. The relationship between duty ratio and dilution rate.

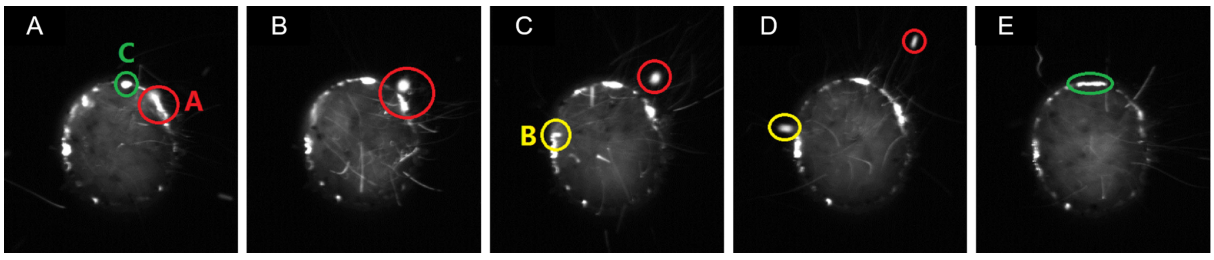

Figure 24. Slag trajectory in the molten pool in the pulsed laser cladding at 0.327-0.329s.

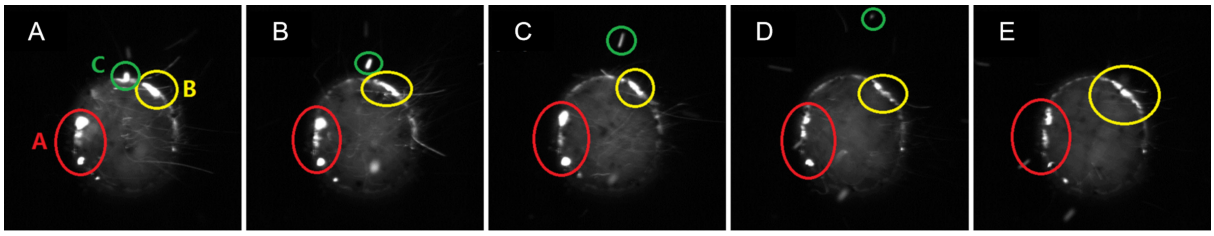

Figure 25. Slag trajectory in the molten pool in the pulsed laser cladding at 0.540-0.542 s.

the middle of the molten pool and melts into liquid metal, reducing the size of the slag along the edge of the molten pool. The slags on the upper section of the slag block C are separated.

Figure 26 depicts the surface shape of the cladding layer at various frequencies. The surface of the cladding layer below the pulsed laser can be seen to have apparent fish scales corresponding to the pulsed laser switching. The switching time of the pulsed laser decreases as the pulsed laser frequency increases and the distance between the fish scales on the surface decreases. At the same time, as the pulsed laser frequency increases from 13.33 Hz to 25 Hz, the spherical slag particles scattered on the surface gradually become smaller and less numerous. When the pulsed laser frequency is changed from 25 Hz to 50 Hz, the sharp differences of the spherical particles are difficult to distinguish, so a thorough examination of their surface roughness must also be performed.

Figure 27 depicts the surface morphology of the cladding layer at various duty ratios, with fish scales visible on the surface of the cladding layer. When the duty ratio is increased, the pulsed laser is turned on for a longer time, and the surface fish scale spacing increases. At the same time, when the duty ratio is increased, the number of spherical slag particles scattered on the surface and their size decrease.

Figure 28A shows the measured surface roughness range of the processed part under different frequencies when the duty ratio is 1:1, with the gray area representing the range of the roughness of each piece of the straight line taken and the dot representing the average value of the required line roughness Ra. The average surface roughness of the cladding layer decreases as the pulsed laser frequency increases from 13.33 Hz to 25 Hz, with a larger decrease; however, the surface roughness increases when the pulsed laser frequency exceeds 50 Hz. It can be observed that when the pulsed laser frequency is increased to 50Hz, the value of surface roughness is comparable to the value at 20 Hz and exceeds the average value of Ra at 25 Hz. The final pulsed laser frequency is around 25 Hz, which improves the cladding layer quality. This shows that increasing the pulsed laser frequency does not further improve the surface finish.

Figure 28B shows the surface roughness of the processed parts at different duty ratios for a pulsed laser frequency of 13.33 Hz. As the duty ratio increases from 1:1 to 3:1, the surface roughness decreases, but the degree of reduction becomes slower. At a duty ratio of 3:1, the quality of the cladding layer improved, with an average Ra of 9.435 μm. The surface tension determines the surface quality when the duty ratio is changed. Because the pulsed laser frequency is the same, the laser beam has the same number of impacts on the molten pool. The lower the surface tension, the less restriction on the shock effect, the higher the fluctuation of the liquid/gas interface, and the easier it is to assimilate molten slag particles. When the duty ratio is increased to a certain point, too low surface tension creates an accumulation of slag particles at the edge of the molten pool, resulting in poor surface quality. A too-large duty ratio causes the pulsed laser to gradually approach the continuous laser, which is detrimental to the surface quality of the cladding layer.

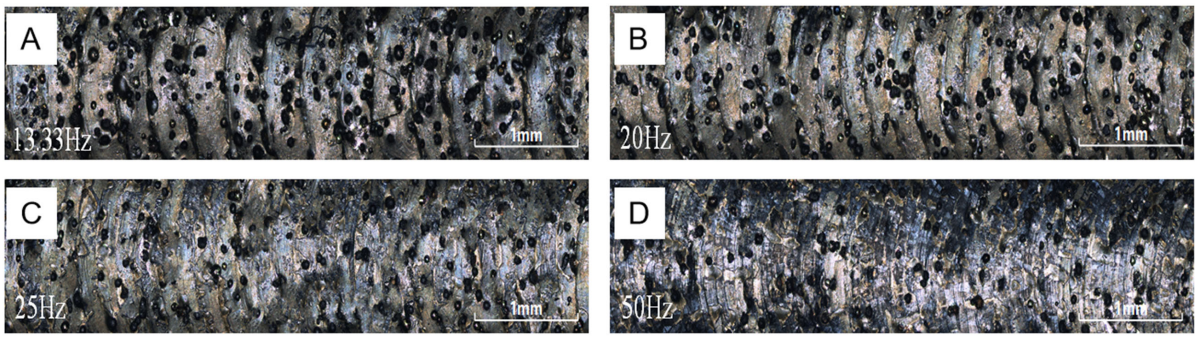

Figure 26. Surface morphology of the cladding layer at different frequencies. (A) 13.33 Hz; (B) 20 Hz; (C) 25 Hz; (D) 50 Hz.

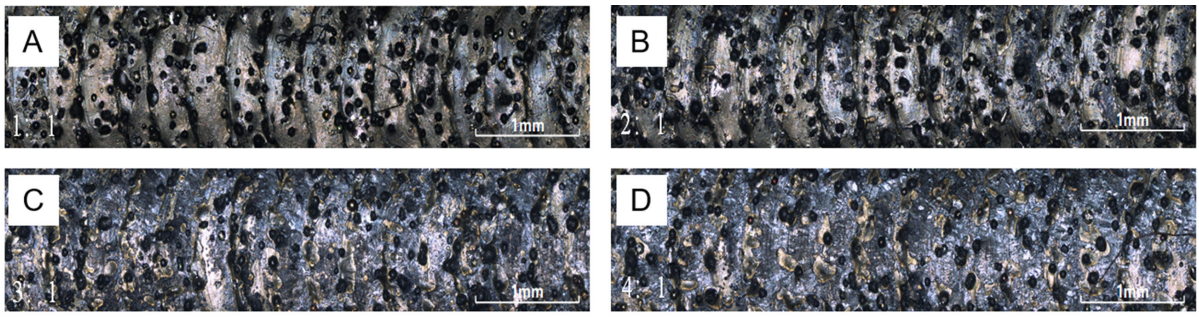

Figure 27. Surface morphology of the cladding layer at different duty ratios. (A) 1:1; (B) 2:1; (C) 3:1; (D) 4:1.

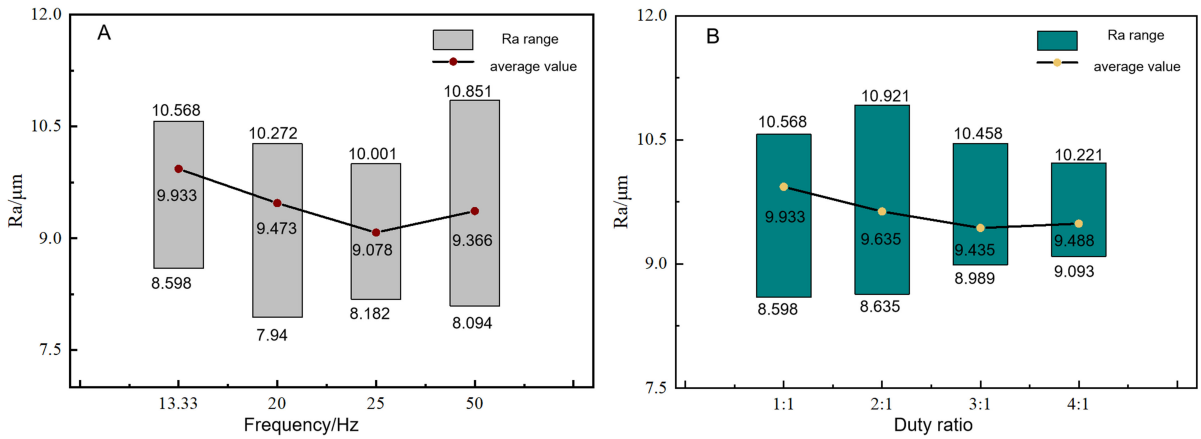

Figure 28. Surface roughness of cladding layer under different parameters. (A) Different frequencies; (B) different duty ratios.

CONCLUSION

A multiphase numerical model of pulsed LC was developed for laser additive remanufacturing processes. The relationship between the laser process parameters and the final bath characteristics was established by simultaneous experimental monitoring and numerical simulations, and the relationship between different parameters and the flow and surface morphology was analyzed, leading to the following conclusions:

Under the numerical model, the height of the cladding layer was 0.651 mm, the width was 3.312 mm, and the penetration depth was 0.147 mm. The measured height of the cladding layer is 0.608 mm, the width is 2.896 mm, and the penetration depth is 0.138 mm. The relative errors were 7.07%, 14.36%, and 6.52%, respectively. The range of relative error between the simulated and experimental temperatures measured with the pyrometer is 0.82% to 28.50%, respectively. Therefore, the numerical model can be a good substitute for the experimental results.

The periodic variations of the molten pool got denser as the pulsed laser frequency increased, and the maximum velocity of the molten pool surface steadily lowered. Because the pulsed laser frequency was too high, the heat input into the molten pool by the external laser heat source was insufficient, the surface tension was excessive, and the liquid metal was difficult to flow. As the duty ratio increased, the interval between molten pool cycles decreased rapidly, and the maximum flow velocity at the surface of the molten pool gradually increased. Since the heat input into the molten pool from the external laser heat source increased as the duty ratio increased, the temperature rose, the surface tension decreased, and the flow velocity increased.

The changing trend of the height of the cladding layer corresponded to the changing trend of heat accumulation in the molten pool, and the breadth and penetration depth of the cladding layer was dictated by the size of the heat-affected zone. The dilution rate was 3.04% at a pulsed laser frequency of 50 Hz. If the pulsed laser frequency exceeded 50 Hz, the metallurgical link between the cladding layer and the substrate became poor. When the duty ratio was larger than 4:1, the likelihood of over-melting increased, affecting the substrate properties.

The smallest average Ra value of 9.078 μm was obtained for a pulsed laser frequency of 25 Hz, while the smallest average Ra value of 9.435 μm was obtained for a duty ratio of 3:1. The optimal surface finish of the cladding layer was obtained with this parameter, providing a fiduciary basis for improving the quality of the material formed.

The mechanism of the pulsed laser acting on the molten pool was well studied to better understand the pulsed LC process and to provide a theoretical model basis for the subsequent choice of laser parameters and the final performance of the parts in the pulsed LC process. However, much about the details of the technique remains to be investigated in the future. For example, future investigations will focus on the interaction mechanism of pulsed laser beams with surface materials and remanufactured powders and on the development of an online quality closed-loop control process for laser remanufacturing.

DECLARATIONS

Authors' contributions

Conceptualization, methodology: Zhao Y
Writing-original draft: Zhao Y
Experiments and experimental data analysis: Liu H, Liu B
Technical support: Liu W
Supervision: Liu S, Li T

Availability of data and materials

Not applicable.

Financial support and sponsorship

This research work was supported partially by the National Natural Science Foundation of China (NOs. 52175455 and 51975100) and Fundamental Research Funds for the Central Universities.

Conflicts of interest

All authors declared that there are no conflicts of interest.

Ethical approval and consent to participate

Not applicable.

Consent for publication

Not applicable.

REFERENCES

1. Zhang Y, Huang W. Comparisons of 304 austenitic stainless steel manufactured by laser metal deposition and selective laser melting. *J Manuf Process* 2020;57:324-33. DOI
2. Gong G, Ye J, Chi Y, et al. Research status of laser additive manufacturing for metal: a review. *J Mater Res Techol* 2021;15:855-84. DOI
3. Nankali M, Akbari J, Moradi M, Malekshahi Beiranvand Z. Effect of laser additive manufacturing parameters on hardness and geometry of Inconel 625 parts manufactured by direct laser metal deposition. *Optik* 2022;249:168193. DOI
4. Yang N, Dong H. Parameters mensuration of metal powder flow in laser cladding. *Acta Opt Sin* 2011;31:s100108. DOI
5. Manvatkar V, De A, Debroy T. Spatial variation of melt pool geometry, peak temperature and solidification parameters during laser assisted additive manufacturing process. *Mater Sci Technol* 2015;31:924-30. DOI
6. Song B, Yu T, Jiang X, Xi W. Numerical model of transient convection pattern and forming mechanism of molten pool in laser cladding. *Numer Heat Transf Part A Appl* 2019;75:855-73. DOI
7. David S, Debroy T, Bhadeshia H. A fresh beginning. *Sci Technol Weld Join* 2004;9:471. DOI
8. Pinkerton AJ, Li L. An investigation of the effect of pulse frequency in laser multiple-layer cladding of stainless steel. *Appl Surf Sci* 2003;208-209:405-10. DOI
9. Shi J, Zhu P, Fu G, Shi S. Geometry characteristics modeling and process optimization in coaxial laser inside wire cladding. *Opt Laser Technol* 2018;101:341-8. DOI
10. Peng X, Kong L, Chen Y, Shan Z, Qi L. Design of a multi-sensor monitoring system for additive manufacturing process. *Nanomanuf Metrol* 2020;3:142-50. DOI
11. Davoudinejad A, Doagou-rad S, Tosello G. A finite element modeling prediction in high precision milling process of aluminum 6082-T6. *Nanomanuf Metrol* 2018;1:236-47. DOI
12. Pekkarinen J, Salminen A, Kujanpää V. Laser cladding with scanning optics: effect of scanning frequency and laser beam power density on cladding process. *J Laser Appl* 2014;26:032002. DOI
13. Shah K, Pinkerton AJ, Salman A, Li L. Effects of melt pool variables and process parameters in laser direct metal deposition of aerospace alloys. *Mater Manuf Process* 2010;25:1372-80. DOI
14. Xing X, Zhou Q, Wang S, Wang L, Jiang F. Numerical investigation of transient temperature distribution during Ti-6Al-4V selective laser melting. *J Therm Sci* 2019;28:370-7. DOI
15. Yazar KU, Pawar S, Park KS, Choi SH. Effect of process parameters on the clad morphology, microstructure, microtexture, and hardness of single layer 316L stainless steel during direct energy deposition. *Mater Charact* 2022;191:112148. DOI
16. Wu J, Zhang C, Jiang P, Li C, Cao H. A prediction approach of fiber laser surface treatment using ensemble of metamodels considering energy consumption and processing quality. *Green Manuf Open* 2022;1:3. DOI
17. Song B, Yu T, Jiang X, Xi W, Lin X. Effect of laser power on molten pool evolution and convection. *Numer Heat Transf Part A Appl* 2020;78:48-59. DOI
18. Tian H, Chen X, Yan Z, Zhi X, Yang Q, Yuan Z. Finite-element simulation of melt pool geometry and dilution ratio during laser cladding. *Appl Phys A* 2019:125. DOI
19. Sergeev D, Marinin E, Kokorin V, Anufriev D. The improvement of surface quality characteristics after mechanical treatment by pulse laser radiation. *Mater Today Proc* 2021;38:1613-6. DOI
20. Wei K, Lv M, Zeng X, et al. Effect of laser remelting on deposition quality, residual stress, microstructure, and mechanical property of selective laser melting processed Ti-5Al-2.5Sn alloy. *Mater Charact* 2019;150:67-77. DOI

21. Wu D, Lu F, Zhao D, et al. Effect of doping SiC particles on cracks and pores of Al_2O_3-ZrO_2 eutectic ceramics fabricated by directed laser deposition. *J Mater Sci* 2019;54:9321-30. DOI
22. Bai Y, Zhao C, Wang D, Wang H. Evolution mechanism of surface morphology and internal hole defect of 18Ni300 maraging steel fabricated by selective laser melting. *J Mater Process Technol* 2022;299:117328. DOI
23. Li L, Gong J, Xia H, et al. Influence of scan paths on flow dynamics and weld formations during oscillating laser welding of 5A06 aluminum alloy. *J Mater Res Technol* 2021;11:19-32. DOI
24. Qi H, Mazumder J, Ki H. Numerical simulation of heat transfer and fluid flow in coaxial laser cladding process for direct metal deposition. *J Appl Phys* 2006;100:024903. DOI
25. Song L, Wang F, Li S, Han X. Phase congruency melt pool edge extraction for laser additive manufacturing. *J Mater Process Technol* 2017;250:261-9. DOI
26. Gharbi M, Peyre P, Gorny C, et al. Influence of a pulsed laser regime on surface finish induced by the direct metal deposition process on a Ti64 alloy. *J Mater Process Technol* 2014;214:485-95. DOI
27. Gharbi M, Peyre P, Gorny C, et al. Influence of various process conditions on surface finishes induced by the direct metal deposition laser technique on a Ti-6Al-4V alloy. *J Mater Process Technol* 2013;213:791-800. DOI
28. Tang Z, Liu W, Zhang N, Wang Y, Zhang H. Real-time prediction of penetration depths of laser surface melting based on coaxial visual monitoring. *Opt Lasers Eng* 2020;128:106034. DOI
29. Ding X, Koizumi Y, Wei D, Chiba A. Effect of process parameters on melt pool geometry and microstructure development for electron beam melting of IN718: a systematic single bead analysis study. *Addit Manuf* 2019;26:215-26. DOI
30. Bhatnagar S, Mullick S, Gopinath M. A lumped parametric analytical model for predicting molten pool temperature and clad geometry in pre-placed powder laser cladding. *Optik* 2021;247:168015. DOI
31. Lin J. Temperature analysis of the powder streams in coaxial laser cladding. *Opt Laser Technol* 1999;31:565-570. DOI
32. Padhi UP, Singh AP, Joarder R. Experimental and numerical investigations of double pulse laser energy deposition in air. *Int J Heat Fluid Flow* 2020;82:108563. DOI
33. Pinkerton AJ, Li L. The effect of laser pulse width on multiple-layer 316L steel clad microstructure and surface finish. *Appl Surf Sci* 2003;208-209:411-6. DOI
34. Wei S, Wang G, Shin YC, Rong Y. Comprehensive modeling of transport phenomena in laser hot-wire deposition process. *Int J Heat Mass Transf* 2018;125:1356-68. DOI
35. Liu H, Li M, Qin X, Huang S, Hong F. Numerical simulation and experimental analysis of wide-beam laser cladding. *Int J Adv Manuf Technol* 2019;100:237-249. DOI
36. Yan Z, Song L, Liu W, Zou X, Zhou X. Numerical analysis of thermal stress evolution of pulsed-wave laser direct energy deposition. *Int J Adv Manuf Technol* 2021;115:1399-410. DOI